NASA's Double Asteroid Redirection Test (DART): Mutual Orbital Period Change Due to Reshaping in the Near-Earth Binary Asteroid System (65803) Didymos

Ryota Nakano, Masatoshi Hirabayashi, Harrison F Agrusa, Fabio Ferrari, Alex J Meyer, Patrick Michel, Sabina D Raducan, Paul Sánchez, Yun Zhang

The Planetary Science Journal, 3:148 (16pp), 2022 July https://doi.org/10.3847/PSJ/ac7566

NASA's Double Asteroid Redirection Test (DART): Mutual Orbital Period Change Due to Reshaping in the Near-Earth Binary Asteroid System (65803) Didymos

Ryota Nakano[1], Masatoshi Hirabayashi[2], Harrison F. Agrusa[3], Fabio Ferrari[4], Alex J. Meyer[5], Patrick Michel[6], Sabina D. Raducan[4], Paul Sánchez[7], and Yun Zhang[6,8]
[1] Department of Aerospace Engineering, Auburn University, Auburn, AL 36849, USA
[2] Department of Aerospace Engineering, Department of Geosciences, Auburn University, Auburn, AL 36849, USA
[3] Department of Astronomy, University of Maryland, College Park, MD 20742, USA
[4] Space Research and Planetary Sciences, Physics Institute, University of Bern, Bern, 3012, Switzerland
[5] Smead Department of Aerospace Engineering Sciences, University of Colorado Boulder, 3775 Discovery Dr., Boulder, CO 80303, USA
[6] Université Côte d'Azur, Observatoire de la Côte d'Azur, CNRS, Laboratoire Lagrange, Nice, France
[7] Colorado Center for Astrodynamics Research, University of Colorado Boulder, 3775 Discovery Dr., Boulder, CO, USA
[8] Department of Aerospace Engineering, University of Maryland, College Park, MD 20742, USA
Received 2022 February 1; revised 2022 May 30; accepted 2022 May 31; published 2022 July 5

Abstract

The Double Asteroid Redirection Test (DART) is the first planetary defense mission to demonstrate the kinetic deflection technique. The DART spacecraft will collide with the asteroid Dimorphos, the smaller component of the binary asteroid system (65803) Didymos. The DART impact will excavate surface/subsurface materials of Dimorphos, leading to the formation of a crater and/or some magnitude of reshaping (i.e., shape change without significant mass loss). The ejecta may eventually hit Didymos's surface. If the kinetic energy delivered to the surface is high enough, reshaping may also occur in Didymos, given its near-critical spin rate. Reshaping on either body will modify the mutual gravitational field, leading to a reshaping-induced orbital period change, in addition to the impact-induced orbital period change. If left unaccounted for, this could lead to an erroneous interpretation of the effect of the kinetic deflection technique. Here we report the results of full two-body problem simulations that explore how reshaping influences the mutual dynamics. In general, we find that the orbital period becomes shorter linearly with increasing reshaping magnitude. If Didymos's shortest axis shrinks by ∼0.7 m, or Dimorphos's intermediate axis shrinks by ∼2 m, the orbital period change would be comparable to the Earth-based observation accuracy, ∼7.3 s. Constraining the reshaping magnitude will decouple the reshaping- and impact-induced orbital period changes; Didymos's reshaping may be constrained by observing its spin period change, while Dimorphos's reshaping will likely be difficult to constrain but will be investigated by the ESA's Hera mission that will visit Didymos in late 2026.

Unified Astronomy Thesaurus concepts: Asteroid satellites (2207); Near-Earth objects (1092); Asteroid dynamics (2210); Asteroid rotation (2211); Two-body problem (1723); Gravitational interaction (669); Planetary structure (1256); Planetary science (1255)

1. Introduction

Launched on 2021 November 24 (UTC), NASA's Double Asteroid Redirection Test (DART) is the first planetary defense mission that examines asteroid deflection capability by kinetic impact for purely scientific purposes (Cheng et al. 2018). The target asteroid is the near-Earth binary asteroid system (65803) Didymos, which consists of a fast-spinning primary named Didymos and a smaller secondary named Dimorphos. With its current trajectory, the spacecraft will impact Dimorphos's leading hemisphere with a relative speed of ∼6.15 km s^{-1} on 2022 September 26 (UTC; Richardson et al. 2022). Prior to impact, the spacecraft will deploy a 6U CubeSat named the Light Italian CubeSat for Imaging of Asteroids (LICIACube) managed by the Italian Space Agency (Dotto et al. 2021). LICIACube will observe the impact event and conduct measurements of the impact crater and ejecta as it flies by the system (Cheng et al. 2020; Dotto et al. 2021). Four years after the impact, the European Space Agency's (ESA) Hera spacecraft will rendezvous with the Didymos system to further analyze the dynamical and geophysical changes caused by the impact, as well as fully characterize the surface, subsurface, and internal properties of the asteroids with its two CubeSats, Juventas and Milani (Michel et al. 2018, 2022). These collaborative missions form the Asteroid Impact and Deflection Assessment cooperation between NASA and ESA (Cheng et al. 2018).

Radar and light-curve observations have constrained Didymos's general shape and spin period. It appears to have a spinning-top shape (a spheroidal object having an equatorial ridge) with a diameter of 780 m (Michel et al. 2016; Naidu et al. 2020). The spin period is 2.26 hr, close to the observed asteroid spin barrier for self-gravitating cohesionless aggregates, so-called rubble piles (Pravec et al. 2006; Zhang et al. 2017, 2021). On the other hand, Dimorphos's shape is largely uncertain at present. As is the case for many binary systems, however, it is expected to be elongated (Pravec et al. 2016); thus, a triaxial ellipsoid with dimensions of 208 m × 160 m × 133 m is currently employed as a design reference asteroid (DRA; DART mission internal document). Dimorphos is assumed to be tidally locked (Pravec et al. 2006; Scheeres 2009; Scheirich & Pravec 2009; Fang 2011; Pravec et al. 2016), which means that its spin period and mutual orbital

Table 1
Physical Parameters and Dynamically Relaxed Nominal Initial Conditions

Parameter	Value	Unit	Reference/Notes
System			
Mass	$(5.55 \pm 0.42) \times 10^{11}$	kg	Derived
Mutual orbital period	11.9216287 ± 0.0000031	hr	Measured (Naidu et al. 2020)
Didymos			
Diameter	780 ± 30	m	Measured (Naidu et al. 2020)
Dimension	$832 \times 837 \times 786$	m	Derived (Naidu et al. 2020)
Mass	5.2280×10^{11}	kg	Derived
Bulk density	2170 ± 350	kg m^{-3}	Derived
Spin period	2.2600 ± 0.0001	hr	Measured (Pravec et al. 2006)
Dimorphos			
Diameter	164 ± 18	m	Derived (Naidu et al. 2020)
Dimension	$208 \times 160 \times 133$	m	Derived (Naidu et al. 2020)
Mass	4.8417×10^{9}	kg	Derived
Bulk density	2170 ± 350	kg m^{-3}	Assumed to be the same as Didymos
Spin period	11.9216287 ± 0.0000031	hr	Assumed
Nominal initial conditions (Agrusa et al. 2020)			
System mass	5.276428×10^{11}	kg	
Didymos mass	5.228011×10^{11}	kg	
Dimorphos mass	4.841661×10^{9}	kg	
Didymos bulk density	2103.4	kg m^{-3}	
Dimorphos bulk density	2103.4	kg m^{-3}	
Separation	1.18	km	
Relative velocity	0.17275	m s^{-1}	Expressed in Didymos-fixed frame
Didymos angular velocity	7.7227×10^{-4}	rad^{-1}	Expressed in Didymos-fixed frame
Dimorphos angular velocity	1.4640×10^{-4}	rad^{-1}	Expressed in Dimorphos-fixed frame

period are approximately equal, 11.92 hr (Naidu et al. 2020). Unlike Didymos, the shape and low spin rate of Dimorphos combine to be well below the theoretical hydrostatic instability limit (Naidu et al. 2020). The mutual orbit is tight, ∼1180 m separation between the center of mass of the bodies. The semimajor axis is expected to be secularly changing at $\dot{a} = -0.076$ cm yr^{-1} (Scheirich & Pravec 2009; Agrusa et al. 2021) due to a combination of binary YORP (BYORP; Ćuk & Burns 2005) and tides (Goldreich & Sari 2009). Importantly, Keplerian point-mass assumptions cannot adequately describe the mutual dynamics of the Didymos system because of the nonspherical shapes and close proximity of the bodies. In fact, the bodies' translational and rotational dynamics are highly coupled; this is known as the full two-body problem (F2BP; Maciejewski 1995; Tricarico 2008; Scheeres 2009). We expect that the Didymos system is currently in or close to a dynamically relaxed state; thus, the mutual orbit should be circular, and the libration (Murray & Dermott 1999) of Dimorphos should be minimum (Agrusa et al. 2020, 2021). Numerical *N*-body discrete element model simulations have shown that Dimorphos's shape is stable in the nominal relaxed preimpact state, both in case the body is a fully fragmented rubble pile and in case it has some structural coherence (Richardson et al. 2022). The same is not true for Didymos, which has a much higher spin rate and requires structural coherence (e.g., cohesive strength of ∼25 Pa for the bulk density of 2170 kg m^{-3}) to maintain its shape (Hirabayashi et al. 2022). The physical parameters of the Didymos system and the dynamically relaxed, nominal initial conditions that approximately put the system on a circular orbit are summarized in Table 1.

Given the ∼11.92 hr nominal orbital period (Naidu et al. 2020), a 10% change in the true anomaly of Dimorphos relative to the nominal case after 1 month from the impact is deemed observable (Rivkin et al. 2021). Therefore, DART is required to cause at least a 73 s orbital period change, which is defined as one of the DART level 1 requirements (Rivkin et al. 2021). The effectiveness of the kinetic deflection technique is quantified by the momentum transfer enhancement factor, "beta" ($\beta \geqslant 1$), which can be estimated from the orbital period change measured by Earth-based telescopes (Rivkin et al. 2021). The β is expected to be in a range from 1 to 5, depending on Dimorphos's structural properties and impact conditions (Stickle et al. 2022). In addition to the orbital period change, the impact may also modify Dimorphos's attitude dynamics. Recent studies suggest that depending on its semiaxis lengths and β, Dimorphos can enter a chaotic tumbling state (Agrusa et al. 2021). Furthermore, the orbital period may fluctuate in response to Dimorphos's libration, which potentially poses a challenge to the orbital period change measurement (Meyer et al. 2021). Both Agrusa et al. (2021) and Meyer et al. (2021) have established that the shape of Dimorphos has major implications for the system's dynamics, with moderately different shapes leading to significantly different dynamics. The shape and postimpact attitude dynamics of Dimorphos are expected to be constrained by ESA's Hera mission (Michel et al. 2022).

Not only does the DART impact change the mutual dynamics (i.e., orbital period change, attitude excitation, etc.; Rivkin et al. 2021; Agrusa et al. 2020, 2021; Meyer et al. 2021), it also modifies the geophysical conditions of the bodies. The impact excavates Dimorphos's surface/subsurface materials and develops a crater (e.g., Stickle et al. 2017, 2022; Rainey et al. 2020; Raducan et al. 2019, 2020). Although its magnitude is uncertain, reshaping (i.e., shape change without significant mass loss) may also occur depending on Dimorphos's structural and impact conditions (Raducan & Jutzi 2022). Moreover, the excavated materials ejected from the impact site

will evolve within the system (Yu et al. 2017; Yu & Michel 2018; Hirabayashi et al. 2022) and may eventually fall onto Didymos, delivering some amount of kinetic energy to the body. The fact that Didymos appears to have a spinning-top shape suggests that Didymos could have gone through a rotationally induced evolution, as seen on Ryugu and Bennu (e.g., Watanabe et al. 2019; Scheeres et al. 2019; Hirabayashi et al. 2020). It also suggests that Didymos may be prone to structural failure due to fast spin at present. Therefore, rotation-driven reshaping could be triggered by small perturbations, especially if ejecta delivers high kinetic energy (Hirabayashi et al. 2017, 2019). Such reshaping on either Didymos or Dimorphos will modify the mutual gravitational field, leading to an orbital period change, in addition to the impact-induced orbital period change. Therefore, the Earth-based observations require careful assessment to determine the orbital period change caused by the DART impact and that by reshaping; otherwise, the evaluation of the kinetic deflection technique using β potentially becomes unreliable.

The main purpose of the present study is to statistically investigate the effect of reshaping on the mutual dynamics, specifically the mutual orbital period. Earlier studies of the structural conditions of top-shaped asteroids (e.g., Hirabayashi & Scheeres 2014; Hirabayashi 2015; Hirabayashi et al. 2020) suggest that Didymos would become a more oblate shape if it experienced rotation-driven reshaping (Hirabayashi et al. 2017, 2019). Dimorphos's reshaping mode is uncertain, so we consider that an idealized impact, where the spacecraft impacts the center of the figure of Dimorphos's leading hemisphere along its intermediate axis, makes Dimorphos reshape such that its intermediate axis becomes shorter than the original, while the other axes become longer. This reshaping mode is reasonable even for the actual DART impact, which will have small ($\sim$10°) nonplanar and in-plane impact angles (Richardson et al. 2022; Raducan & Jutzi 2022). Assuming that reshaping occurs instantaneously after the impact, we generate a number of synthetic shape models of a reshaped Didymos and Dimorphos. Both bodies are treated as rigid bodies, and the mutual dynamics are propagated for 180 days after the instantaneous reshaping event for each shape. For this, we employ a finite element modeling (FEM) approach F2BP model (hereafter F2BPFEM; Yu et al. 2019; Gao et al. 2022), which gives results consistent with the General Use Binary Asteroid Simulator (GUBAS), a well-validated F2BP simulation package developed by Davis & Scheeres (2020, 2021). In the F2BP simulations, we do not take into account the momentum transferred by the DART impact (i.e., β), which also induces the orbital perturbation; this is because the reshaping and impact effects are assumed to be independent to first order, so whether or not the momentum change is included should not affect the reshaping effect we aim to quantify. For the effect of noninstantaneous, long-term reshaping of the bodies on the mutual dynamics, we refer readers to the companion paper, which treats one or both bodies as a rubble pile by using N-body granular physics codes (Agrusa et al. 2022).

2. Approach

In the following sections, we first introduce F2BPFEM and simulate the nominal dynamics of the Didymos system, i.e., the dynamics without reshaping in either Didymos or Dimorphos. We also demonstrate that F2BPFEM gives results consistent with GUBAS. Next, to quantify the reshaping, we define "reshaping parameters," which describe the ratios of the reshaped body's semiaxes to its original semiaxes. Lastly, we present Didymos's and Dimorphos's synthetic shape model generation processes and how we conduct F2BP simulations.

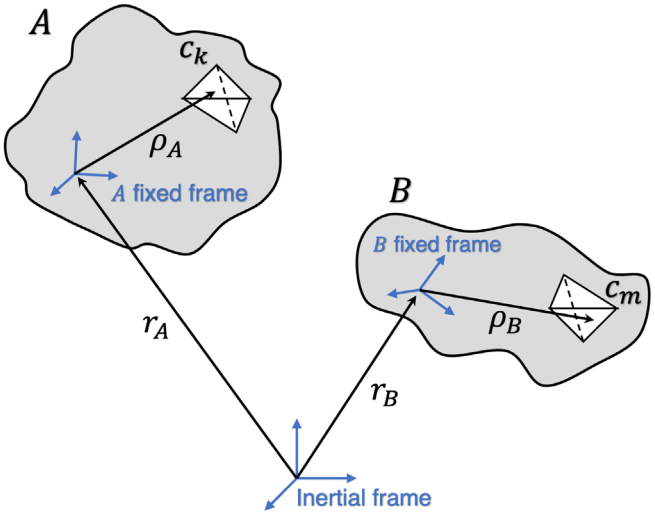

Figure 1. System with two arbitrary homogeneous rigid bodies.

2.1. FEM Approach F2BP Model

To describe the F2BP dynamics (e.g., Werner & Scheeres 2005; Fahnestock & Scheeres 2006; Hirabayashi & Scheeres 2013), we employ an FEM approach (Yu et al. 2019; Gao et al. 2022). A system consisting of two arbitrary rigid bodies A and B having uniform mass distribution over their entire volumes is illustrated in Figure 1. In the FEM approach, the volumes of the two bodies are filled with tetrahedral elements. The mutual potential between arbitrary tetrahedral elements c_k in A and c_m in B is given by

$$U_{km} = \iiint_{c_m} \iiint_{c_k} \frac{-G\sigma_{c_k}\sigma_{c_m}}{|\boldsymbol{r}_B + \boldsymbol{\rho}_B - \boldsymbol{r}_A - \boldsymbol{\rho}_A|} \times dx_a dy_a dz_a dx_b dy_b dz_b, \quad (1)$$

where G is the gravitational constant; σ_{c_k} and σ_{c_m} are the densities of c_k and c_m, respectively; and $\boldsymbol{\rho}_A = (x_a, y_a, z_a)$ and $\boldsymbol{\rho}_B = (x_b, y_b, z_b)$ are the position vectors of any point inside c_k in the body A fixed frame and any point inside c_m in the body B fixed frame, respectively. Finally, $\boldsymbol{r}_A$ and $\boldsymbol{r}_B$ are the position vectors of the centroid of A and B, respectively.

Using a bilinear interpolation technique, Equation (1) can be approximated as

$$U_{km} \approx \hat{U}_{km} = \frac{1}{576} J_k^{-1} J_m^{-1} \sum_i \sum_j U_{ij}^{km}, \quad (2)$$

where U_{ij}^{km} is the value of the integrand of Equation (1) at four corners, $i = 1, \ldots, 4$ in c_k and $j = 1, \ldots, 4$ in c_m, expressed in the tetrahedral natural coordinates. Here J_k and J_m are the Jacobian determinants associated with the coordinate transformation (Yu et al. 2019). See Appendix A for the definition of the natural coordinates and the Jacobian formulation. Assembling the tetrahedral elements over two bodies, we have the total value of

Table 2
Summary of the Symbols Used

Symbol	Description
G	Gravitational constant
A	Rigid body A
B	Rigid body B
c_k	Tetrahedral element in A
c_m	Tetrahedral element in B
σ_{c_k}	Density of c_k
σ_{c_m}	Density of c_m
$\boldsymbol{r}_A$	Position vector of the centroid of A
$\boldsymbol{r}_B$	Position vector of the centroid of B
$\boldsymbol{\rho}_A$	Position vector of any point inside of c_k
$\boldsymbol{\rho}_B$	Position vector of any point inside of c_m
J_k, J_m	Jacobians for the coordinate transformation
U_{km}	Mutual potential between c_k and c_m
$\hat{U}_{km}$	Approximation of U_{km} in natural coordinates
U	Mutual potential

the mutual potential, U, as

$$U \approx \sum_{c_k \in A} \sum_{c_m \in B} \hat{U}_{km}. \tag{3}$$

Unlike other F2BP modeling approaches, which often use series expansions with an infinite number of terms, there are only a finite number of summations in Equation (3). Therefore, the FEM approach does not have gravity order truncation, although the approximation accuracy depends on, for example, the number of tetrahedral elements in each body and shape function used in the FEM interpolation (Yu et al. 2019). Additionally, we note that FEM techniques are often used in structural and thermophysical analyses (e.g., Hirabayashi & Scheeres 2014; Nakano & Hirabayashi 2021); the FEM approach presented here can be combined with other FEM models to investigate complex F2BP dynamics coupled with the structural and/or thermophysical conditions of the bodies. The symbols used in Equations (1)–(3) are summarized in Table 2. The FEM expressions of the total attraction force acting on A and torques acting on A and B can be obtained to formulate the equations of motion of the two bodies, which are given in Appendix B.

F2BPFEM has been implemented in C++, with MPI for parallelization (Nakano et al. 2020). It takes the FEM (4-node tetrahedral element) shape models of the primary and secondary along with the system's initial conditions, physical parameters, and integrator settings as inputs, integrates the equations of motion, and outputs states and energies at each time step.

We simulate the nominal dynamics of the Didymos system for 180 days using F2BPFEM. Based on Didymos's and Dimorphos's shape models available in DRA, FEM shape models are generated by using tetgen, a publicly available FEM generator (Si 2015). The mesh statistics are summarized in Table 3. We use the nominal initial conditions and physical parameters given in Table 1. A Runge–Kutta fourth-order method (RK4) with a fixed time step of 60 s is employed as the integrator. For comparison, we also conduct simulations by using GUBAS with fourth- and eighth-order gravity truncation settings with the same initial conditions, physical parameters, and integrator settings (RK4 with a fixed time step of 60 s). Note that GUBAS has been extensively used for DART-related mutual dynamics studies (e.g., Agrusa et al. 2020, 2021; Meyer et al. 2021), and GUBAS with a fourth-order gravity truncation setting was determined as sufficient for accurate dynamics modeling (Agrusa et al. 2020).

Table 3
FEM Mesh Statistics

Body	Nodes	Tetrahedral Elements	Average Element Volume
Didymos	4550	24,780	10,000 m^3
Dimorphos	473	2090	1100 m^3

Figure 2(a) shows the evolution of the orbital elements over the first 3 days of the 180 day simulation for F2BPFEM (blue), GUBAS fourth (red), and GUBAS eighth (yellow). All models consistently show osculating orbital elements, highlighting the importance of using F2BP models to describe the mutual dynamics accurately. The differences in the semimajor axis and eccentricity are indistinguishable between F2BPFEM and GUBAS (fourth and eighth), while small differences can be seen in the inclination. The libration with up to $\sim 5^\circ$ amplitude is observed in all models. Because of the difference in mass representation, however, we find that the angular position (i.e., true anomaly) of Dimorphos gradually becomes different between the models. The angular position differences relative to GUBAS fourth are shown in Figure 2(b). The angular positions modeled by F2BPFEM and GUBAS eighth are color coded in blue and red, respectively. We observe that the difference increases with small oscillation as time proceeds. Between F2BPFEM and GUBAS fourth, the difference is $\sim 12^\circ$ at $t = 180$ days, while the difference between F2BPFEM and GUBAS eighth is always less than 2° during the 180 day simulation. Therefore, we anticipate that F2BPFEM (with the FEM shape models given in Table 3) is comparable to GUBAS with an eighth-order gravity truncation setting and conclude that F2BPFEM is useful and can be employed for DART-related mutual dynamics studies. We finally note that several tests have been performed to verify that the FEM shape models with the number of nodes and elements given in Table 3 are sufficient to obtain an accurate result. In general, when the number of nodes in each body is sufficiently large ($\sim$3500 nodes for Didymos; $\sim$350 nodes for Dimorphos), the result does not change significantly.

2.2. Synthetic Shape Model Generation

2.2.1. Reshaping Parameters

We quantify Didymos's and Dimorphos's reshaping by using reshaping parameters, which denote the ratios of a reshaped body's semiaxes to its original semiaxes. Here we give a more precise definition. Consider a body in which a right-handed Cartesian coordinate system $\{x, y, z\}$ is defined such that the x-, y-, and z-axes are aligned with the body's longest, intermediate, and shortest axes, respectively. At the intersections between these axes (in positive and negative directions) and the body's surface, we define six surface points, $+x_0$, $-x_0$, $+y_0$, $-y_0$, $+z_0$, and $-z_0$, as shown in Figure 3. When the body reshapes, the surface points move to new locations: $+x_1$, $-x_1$, $+y_1$, $-y_1$, $+z_1$, and $-z_1$. Given these changes, we define the reshaping parameters as

$$\gamma_{+s} = \frac{\|+s_1\|}{\|+s_0\|}, \quad \text{for positive semiaxis } s, \tag{4}$$

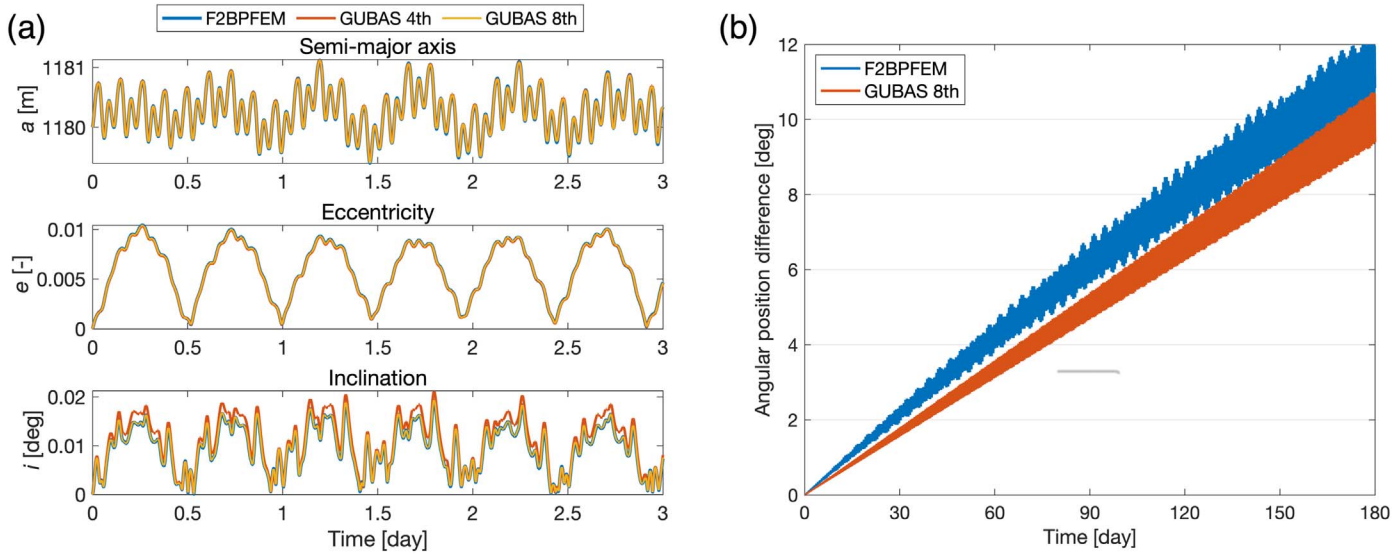

Figure 2. (a) Nominal orbital element evolution over the first 3 days (∼six orbital periods) of the 180 day simulation. The blue, red, and yellow lines indicate F2BPFEM, GUBAS fourth, and GUBAS eighth results, respectively. (b) Angular position difference relative to GUBAS fourth.

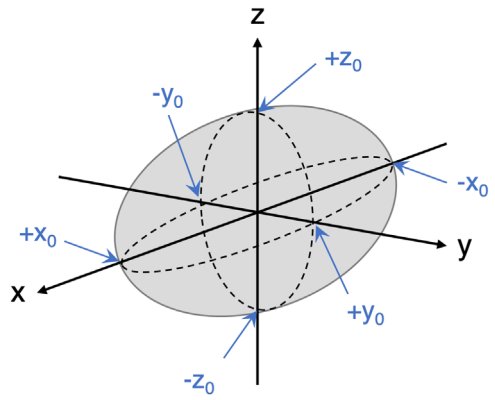

Figure 3. Geometrical definitions, where $\pm x_0$, $\pm y_0$, and $\pm z_0$, indicated by the arrows, are the surface points located at the intersections between the semiaxes ($\pm x$, $\pm y$, $\pm z$) and the body's surface.

$$\gamma_{-s} = \frac{\|-s_1\|}{\|-s_0\|}, \quad \text{for negative semiaxis s,} \tag{5}$$

where $s = (x, y, z)$. Each reshaping parameter describes the ratio of the corresponding semiaxis ($\pm x$, $\pm y$, $\pm z$) of the reshaped body to that of the original body. When generating a reshaped body, we choose six reshaping parameters and modify (i.e., increase or decrease) the corresponding semiaxis length. Example synthetic shape models are given in the following sections (Sections 2.2.2 and 2.2.3). In the discussion hereafter, we add superscripts A and B to $\gamma_{\pm s}$ in order to distinguish $\gamma_{\pm s}$ for Didymos and that for Dimorphos, respectively.

2.2.2. Didymos

Because of the 2.26 hr spin period, the centrifugal acceleration is dominant at low to midlatitudes, resulting in high surface slopes (∼45° to ∼180°; Naidu et al. 2020). Thus, if Didymos's reshaping does occur due to, for example, materials ejected from the impact site falling onto Didymos's surface, the reshaping mode is likely to become a more oblate shape (e.g., Hirabayashi 2015; Hirabayashi et al. 2022; Nakano & Hirabayashi 2020), in other words, outward deformation on the equatorial plane and inward deformation at the polar regions (Hirabayashi et al. 2017, 2019). While the detailed ejecta dynamics are not yet fully constrained (i.e., whether ejecta hits Didymos, and if so, where on the body), we anticipate that the reshaping mode would be similar regardless of where on Didymos's surface the collisions occur. With the reshaping parameters introduced in Section 2.2.1, increasing the oblateness corresponds to $\gamma^A_{\pm x} \geqslant 1$ and $\gamma^A_{\pm y} \geqslant 1$, while $\gamma^A_{\pm z} \leqslant 1$. However, the detailed reshaping conditions would depend on various factors, such as surface/internal structural conditions (e.g., Zhang et al. 2017, 2018) and local topographic features (e.g., Hirabayashi et al. 2019, 2020), as well as other impact-related perturbations (e.g., seismic shaking), which make predicting the detailed reshaping condition difficult. To account for this uncertainty, we set the reshaping parameters randomly but within a bounded range so that the synthetic shape models of the reshaped Didymos reflect the structural simulation results and are physically realistic. This approach also allows us to statistically quantify the most probable effect of Didymos's reshaping on the mutual dynamics.

To generate synthetic shape models, we impose several assumptions. First, given a threshold of reshaping magnitude having a value larger than 1, which we denote as $\gamma^A_{\max}$, we assume that $\gamma^A_{\pm x}$ and $\gamma^A_{\pm y}$ take uniformly random values from 1 to $\gamma^A_{\max}$. Second, Didymos's volume is assumed to remain the same before and after reshaping. Lastly, assuming that impact-related perturbations are not significantly biased to either the northern or southern hemisphere, we set $\gamma^A_{+z} = \gamma^A_{-z}$. Under these assumptions, Didymos's reshaping can be characterized with four reshaping parameters, $\gamma^A_{\pm x}$ and $\gamma^A_{\pm y}$. Figure 4 shows an example synthetic shape model, with the black wire frame representing the original shape. The $\gamma_{\max}$ is set to 1.1. The randomly chosen $\gamma^A_{\pm x}$ and $\gamma^A_{\pm y}$ are 1.07, 1.06, 1.04, and 1.02, respectively. From the constant volume assumption, $\gamma^A_{\pm z}$ is found as 0.91. This implies that the reshaping in the z-axis, $\delta_z = D_0 - D$, where D_0 and D are the z-axis length of the original body and the reshaped body, respectively, is 69.4 m. Note that this is an exaggerated reshaping condition generated specifically for clear visualization.

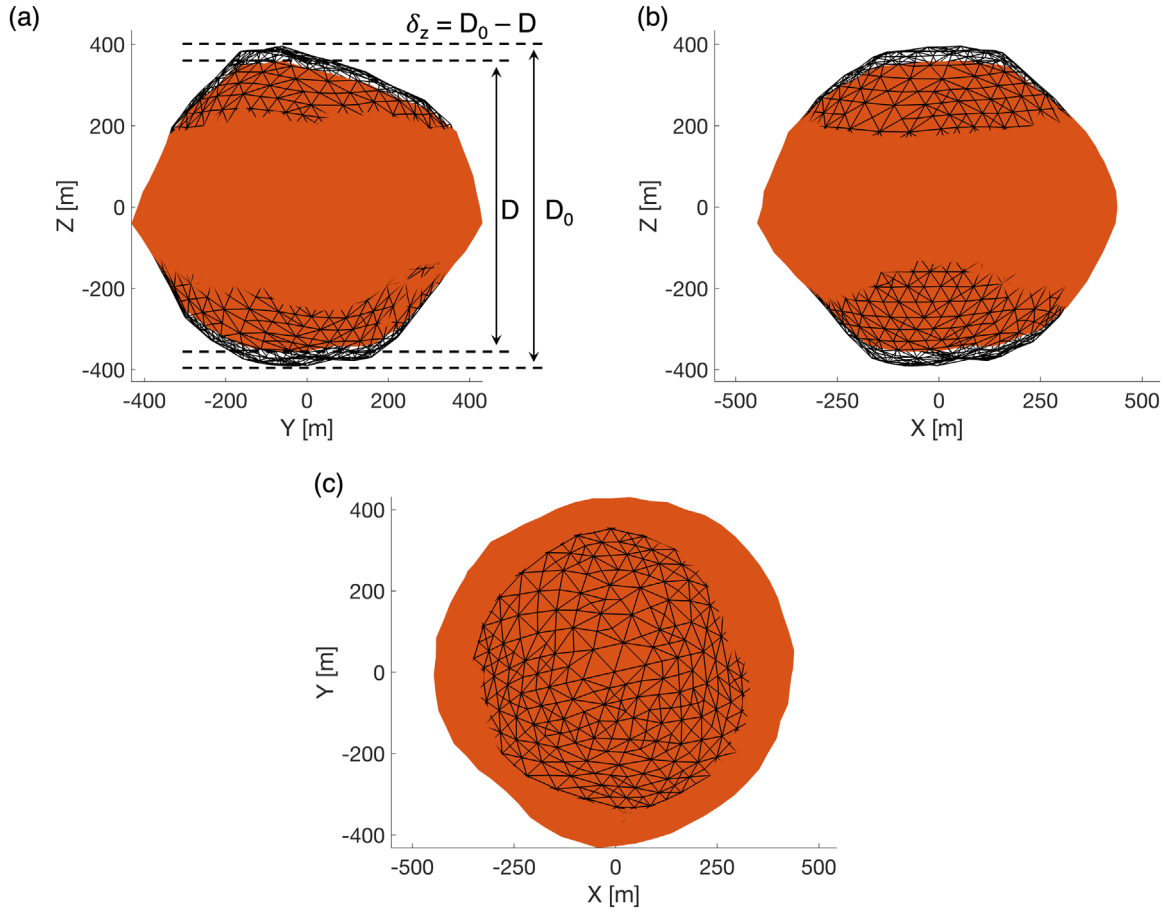

Figure 4. Synthetic shape model of reshaped Didymos. Panels (a) and (b) show the side view from the x- and y-axis, respectively. Panel (c) shows the top-down view. The black wire frame represents the original shape. The reshaping parameters are $[\gamma^A_{+x}, \gamma^A_{-x}, \gamma^A_{+y}, \gamma^A_{-y}, \gamma^A_{+z}, \gamma^A_{-z}] = [1.07, 1.06, 1.04, 1.02, 0.91, 0.91]$. The reshaping in the z-axis, δ_z, is 69.4 m.

We consider 10 different $\gamma^A_{\max}$ cases, from 1.001 to 1.01 in steps of 0.001. For each $\gamma^A_{\max}$ case, we generate 500 sets of $\{\gamma^A_{\pm x}, \gamma^A_{\pm y}\}$. As mentioned above, the values are uniformly randomly chosen from $[1, \gamma^A_{\max})$. (This implies that $\gamma^A_{\pm x}$ and $\gamma^A_{\pm y}$ may take 1 but do note take $\gamma^A_{\max}$.) In total, we have 5000 synthetic shape models. Assuming that reshaping occurs instantaneously, the mutual dynamics are propagated for 180 days after a reshaping event by using F2BPFEM for each shape. The initial conditions are the same as in Table 1. Importantly, however, because the mutual dynamics are reported to be sensitive to small perturbations in the initial conditions (e.g., the initial velocities and rotation phases of the bodies; Agrusa et al. 2020), the initial conditions should be properly set in order to give consistent initial mutual dynamics throughout the 5000 simulations. For each simulation, we thus modify Didymos's initial angular velocity based on the moment of inertia change due to reshaping while assuming that other quantities remain the same to ensure that Didymos's initial angular momentum is the same as the nominal value.

2.2.3. *Dimorphos*

The DART impact will deliver high kinetic energy, 10^{10} J, to Dimorphos (Rivkin et al. 2021). Given that the energy required for catastrophic disruption of Dimorphos is in the range of $\sim 10^{11}-10^{12}$, depending on the body's tensile strength (Jutzi 2015; Richardson et al. 2022), it is possible that not only does the impact excavate Dimorphos's surface/subsurface materials and develop a crater, it induces some magnitude of reshaping (Raducan & Jutzi 2022). Importantly, Dimorphos's reshaping is not induced by rotation; thus, its reshaping mode should be different from Didymos's. To statistically explore the reshaping condition, we generate synthetic shape models of the reshaped Dimorphos. We consider an idealized impact scenario where the spacecraft impacts the center of the figure of Dimorphos's leading hemisphere along its intermediate axis (y-axis), as depicted in Figure 5, although the actual impact will have small nonplanar and in-plane impact angles based on the current spacecraft trajectory (Richardson et al. 2022). We assume that the reshaping occurs such that the $+y$-axis becomes shorter (i.e., $\gamma^B_{+y} < 1$), while the $-y$-axis remains the same (i.e., $\gamma^B_{-y} = 1$) and the $\pm x$- and $\pm z$-axes become longer (i.e., $\gamma^B_{\pm x} > 1$ and $\gamma^B_{\pm z} > 1$). This reshaping mode is inferred based on recent impact modeling work by Raducan & Jutzi (2022). Under constant volume, we assume that $\gamma^B_{\pm x}$ and $\gamma^B_{\pm z}$ take uniformly random values from 1 to $\gamma^B_{\max}$, where $\gamma^B_{\max} > 1$ is the threshold of the reshaping magnitude. Then, Dimorphos's reshaping can be characterized with four reshaping parameters, $\gamma^B_{\pm x}$ and $\gamma^B_{\pm z}$. Figure 6 shows an example synthetic shape model. The black wire frame represents the original shape. The $\gamma^B_{\max}$ is set to 1.1, and $\gamma^B_{\pm x}$ and $\gamma^B_{\pm z}$ are randomly set as 1.05, 1.08, 1.01, and 1.09, respectively. The

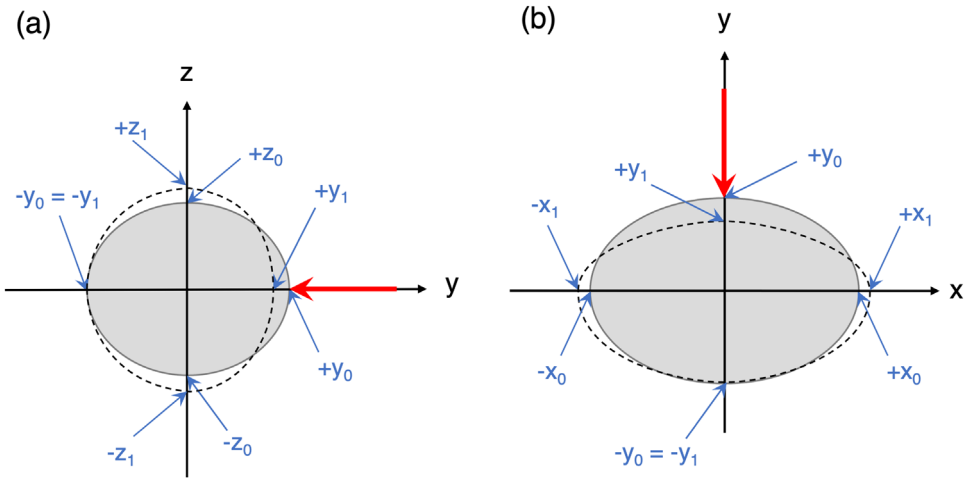

Figure 5. Idealized impact (red arrow) and considered reshaping mode (dashed line). Panels (a) and (b) show the side and top-down view, respectively. Due to the idealized impact, $+y_0$, $\pm x_0$, and $\pm z_0$ move to new locations $+y_1$, $\pm x_1$, and $\pm z_1$, respectively, while $-y_0$ remains the same ($-y_0 = -y_1$).

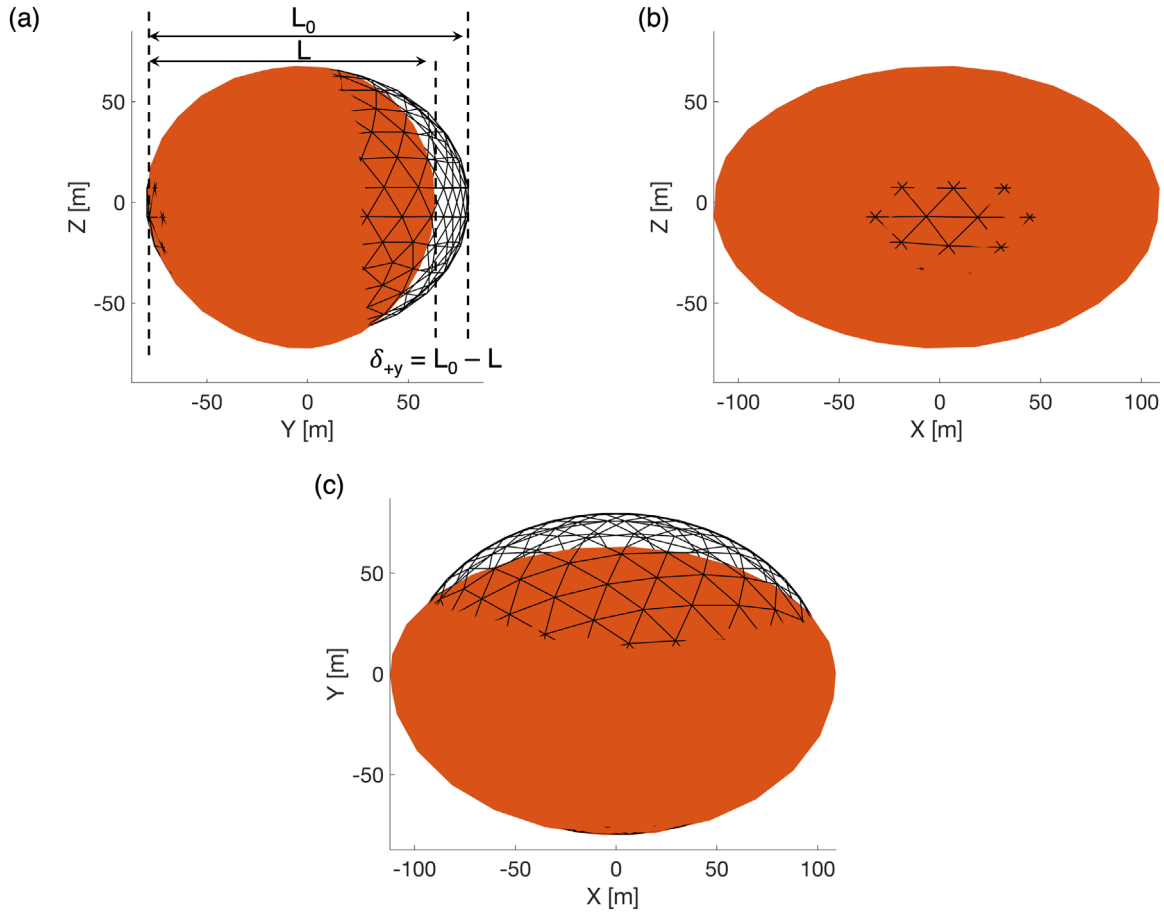

Figure 6. Synthetic shape model of the reshaped Dimorphos. Panels (a) and (b) show the side views from the x- and y-axis, respectively. Panel (c) shows the top-down view. The black wire frame represents the original shape. The reshaping parameters are $[\gamma^B_{+x}, \gamma^B_{-x}, \gamma^B_{+y}, \gamma^B_{-y}, \gamma^B_{+z}, \gamma^B_{-z}] = [1.05, 1.08, 0.79, 1.00, 1.01, 1.09]$. The reshaping in the $+y$, $\delta_{+y} = L_0 - L$, is found to be 16.9 m.

γ^B_{+y} is found as 0.79, which corresponds to ∼17 m of reshaping in $+y$ ($\delta_{+y} =$ ∼17 m).

We consider 10 different $\gamma^B_{\max}$ cases from 1.01 to 1.1 in steps of 0.01. For each $\gamma^B_{\max}$ case, we generate 500 sets of $\{\gamma^B_{\pm x}, \gamma^B_{\pm z}\}$ with the values uniformly randomly chosen from $[1, \gamma^B_{\max})$, totaling 5000 synthetic shape models. The mutual dynamics are propagated for 180 days after the (instantaneous) reshaping event by using F2BPFEM for each shape. The initial conditions are the same as in Table 1; however, again, we modify Dimorphos's initial angular velocity to take into account the change in the moment of inertia of the reshaped Dimorphos. This process ensures that the 5000 simulations start from

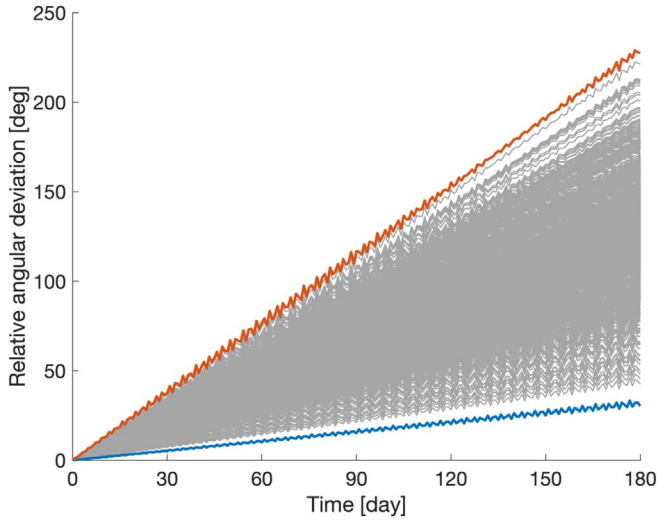

Figure 7. Evolution of the relative angular deviation when Didymos reshapes. All 500 shapes in the $\gamma^A_{\max} = 1.005$ case are plotted (gray lines). The most and least perturbed ones are color coded in red and blue, respectively. The reshaping parameters $[\gamma^A_{+x}, \gamma^A_{-x}, \gamma^A_{+y}, \gamma^A_{-y}]$ for these two shapes are [1.004 3, 1.003 6, 1.004 6, 1.004 8] and [1.001 0, 1.001 4, 1.000 5, 1.001 4], respectively, which correspond to the most and least oblate shapes among the 500 shapes.

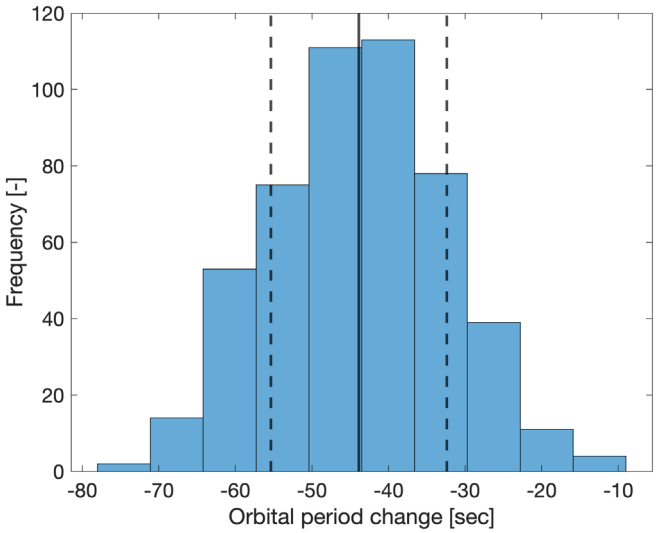

Figure 8. Histogram for the orbital period change when Didymos reshapes. The maximum reshaping parameter is $\gamma^A_{\max} = 1.005$. The black solid and dashed lines indicate the mean and standard deviation, −43.9 and 11.5 s, respectively.

comparable initial mutual dynamics. We note that the actual impact will likely have a small offset from the center of the figure, which may slightly modify the angular momentum. However, the change will be small compared to the original angular momentum. Thus, here we consider that the angular momentum remains the same before and after the impact. Further investigation, including the possible change in Dimorphos's angular momentum due to the impact, is planned once the detailed shape model of Dimorphos and the actual impact condition become available.

3. Results

3.1. Effect of Didymos's Reshaping

The results show that Didymos's reshaping perturbs mutual dynamics. Due to the perturbation, the angular position of Dimorphos gradually deviates from the nominal case. We call this difference the relative angular deviation. Figure 7 shows the evolution of the relative angular deviation over 180 days for all 500 shapes in $\gamma^A_{\max} = 1.005$, which is the moderate reshaping case among the range of $\gamma^A_{\max}$ considered in the present study. We find that with small oscillations, the relative angular deviation linearly increases as time proceeds. All 500 shapes show a positive relative angular deviation at any time. After 180 days from reshaping (at $t = 180$ days), the relative angular deviation reaches 230° at maximum, meaning that Dimorphos is more than a half orbit ahead of where the nominal (without Didymos's reshaping) Dimorphos would be. The reshaping parameters $[\gamma^A_{+x}, \gamma^A_{-x}, \gamma^A_{+y}, \gamma^A_{-y}]$ for the most and least perturbed ones (color coded in red and blue, respectively) are [1.004 3, 1.003 6, 1.004 6, 1.004 8] and [1.001 0, 1.001 4, 1.000 5, 1.001 4], respectively, which correspond to the most and least oblate shapes among the 500 shapes. The distribution of the relative angular deviations at $t = 180$ days is well approximated as Gaussian, with the mean and standard deviation being 134° and 35°, respectively.

Table 4
The Mean and Standard Deviation of the Orbital Period Change for All $\gamma^A_{\max}$ Cases

$\gamma^A_{\max}$ [−]	Mean [s]	1σ [s]
1.001	−8.116	2.350
1.002	−17.01	5.156
1.003	−25.75	7.536
1.004	−35.43	10.36
1.005	−43.87	11.50
1.006	−51.33	15.65
1.007	−61.74	16.14
1.008	−68.84	20.39
1.009	−76.88	21.62
1.010	−84.98	25.61

We can compute the orbital period change relative to the nominal case from the relative angular deviation. The computation process is outlined in Appendix C. Figure 8 shows the histogram for the orbital period change for $\gamma^A_{\max} = 1.005$. We find that the 500 shapes (where $\gamma^A_{\pm x}$ and $\gamma^A_{\pm y}$ are uniformly randomly selected from $[1, \gamma^A_{\max}]$) result in a Gaussian distribution. The most perturbed one (red line in Figure 7) corresponds to an orbital period change of −72 s, while the least perturbed one (blue line in Figure 7) corresponds to an orbital period change of −10 s. The mean and standard deviation are found as −43.9 and 11.5 s, respectively. All 500 shapes show shorter orbital periods compared to the nominal case, as expected from the distribution of the relative angular deviations (Figure 7). Similar results are found in the other $\gamma^A_{\max}$ cases too; regardless of the reshaping condition, the orbital period always becomes shorter than the nominal case. The mean and standard deviations for all $\gamma^A_{\max}$ cases are summarized in Table 4.

Finally, we compute the reshaping in the z-axis, δ_z, for each synthetic shape model and plot the orbital period change as a function of δ_z. In Figure 9, the blue stars are the simulated results and indicate the mean of both the orbital period change

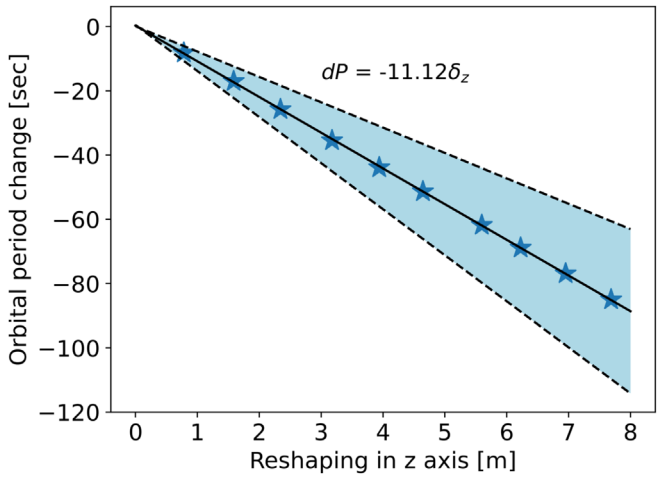

Figure 9. Reshaping in the z-axis (δ_z) vs. orbital period change. The blue stars indicate the simulated results. The black solid line indicates a linear fitted line given by the equation shown in the figure. The blue shaded region represents 1σ in the orbital period change.

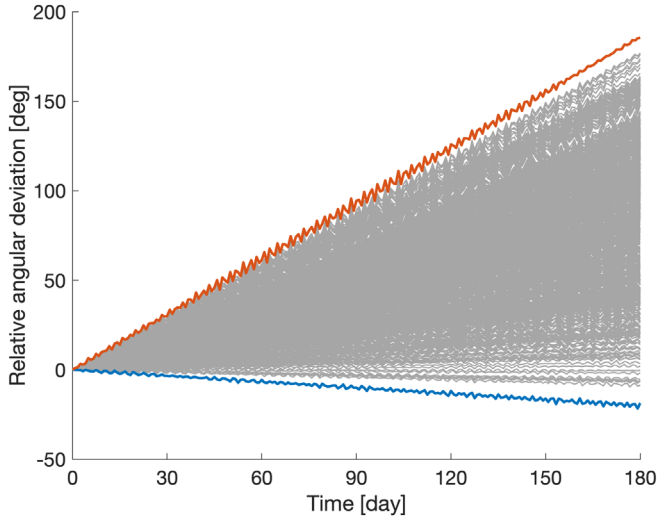

Figure 10. Evolution of the relative angular deviation when Dimorphos reshapes. All 500 shapes in the $\gamma^B_{\rm max} = 1.05$ case are plotted (gray lines). The most perturbed ones in the positive and negative directions are color coded in red and blue, respectively. The reshaping parameters $[\gamma^B_{+x}, \gamma^B_{-x}, \gamma^B_{+z}, \gamma^B_{-z}]$ for these two shapes are [1.049, 1.049, 1.000, 1.033] and [1.001, 1.001, 1.049, 1.041], respectively.

and δ_z for 500 shapes for each $\gamma^A_{\rm max}$ case. We find that the orbital period linearly decreases as δ_z increases. The linear fitted approximation reads $dP = -11.12\delta_z$, where dP denotes the orbital period change. This result suggests that if we can know δ_z, we can estimate the orbital period change due to Didymos's reshaping, although the uncertainty in the orbital period change becomes large as δ_z increases.

3.2. Effect of Dimorphos's Reshaping

The results show that Dimorphos's reshaping also perturbs the mutual dynamics. Figure 10 shows the evolution of the relative angular deviation over 180 days for all 500 shapes in $\gamma^B_{\rm max} = 1.05$. This is the moderate reshaping case among the range of $\gamma^B_{\rm max}$ considered in the present study. Similar to the case of Didymos's reshaping, the relative angular deviation

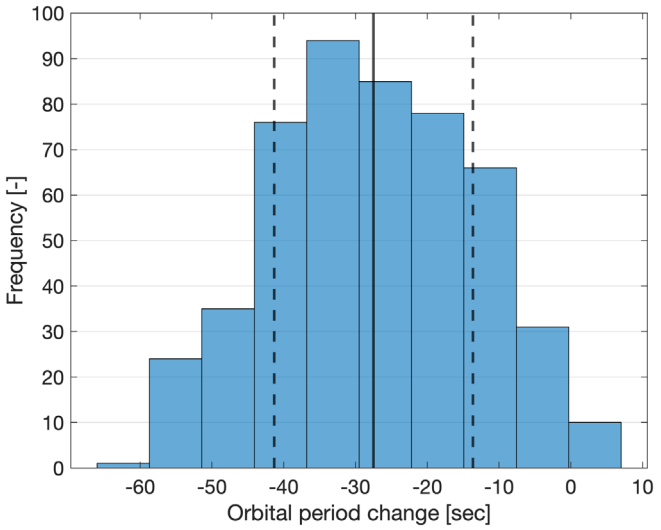

Figure 11. Histogram for the orbital period change when Dimorphos reshapes. The maximum reshaping parameter is $\gamma^B_{\rm max} = 1.05$. The black solid and dashed lines indicate the mean and standard deviation, −27.5 and 13.9 s, respectively.

Table 5
The Mean and Standard Deviation of the Orbital Period Change for All $\gamma^B_{\rm max}$ Cases

$\gamma^B_{\rm max}$ [−]	Mean [s]	1σ [s]
1.01	−5.081	2.462
1.02	−10.55	5.281
1.03	−16.55	8.154
1.04	−22.17	11.06
1.05	−27.49	13.85
1.06	−34.48	16.45
1.07	−39.46	18.85
1.08	−43.44	21.49
1.09	−50.83	25.56
1.10	−55.75	28.14

linearly evolves (with small oscillations) as time proceeds. In the majority of 500 shapes in the $\gamma^B_{\rm max} = 1.05$ case, the relative angular deviation evolves in the positive direction; however, we find that 10 shapes show evolutions in the negative direction. The most perturbed ones in the positive and negative directions, which are color coded in red and blue, reach 186° and −18° at $t = 180$ days, respectively. The distribution at $t = 180$ days is approximately Gaussian, with the mean and standard deviation being 83°.6 and 42°.1, respectively.

We compute the orbital period change from the determined relative angular deviation. Figure 11 shows the histogram for the orbital period change for $\gamma^B_{\rm max} = 1.05$. We again find that the 500 shapes (where $\gamma^B_{\pm x}$ and $\gamma^B_{\pm z}$ are uniformly randomly selected from $[1, \gamma^B_{\rm max})$) result in a Gaussian distribution. The orbital period change varies from −61 to 6 s, and the mean and standard deviation are found as −27.5 and 13.9 s, respectively. While we see that 10 shapes result in a positive orbital period change (i.e., a longer orbital period than the nominal case), those generally fall outside of 2σ. Similar results are observed in the other $\gamma^B_{\rm max}$ cases. The mean and standard deviations for all $\gamma^B_{\rm max}$ cases are summarized in Table 5. We note that among all 5000 shapes, 78 shapes (1.56%) result in longer orbital periods; we find that the orbital period becomes longer when

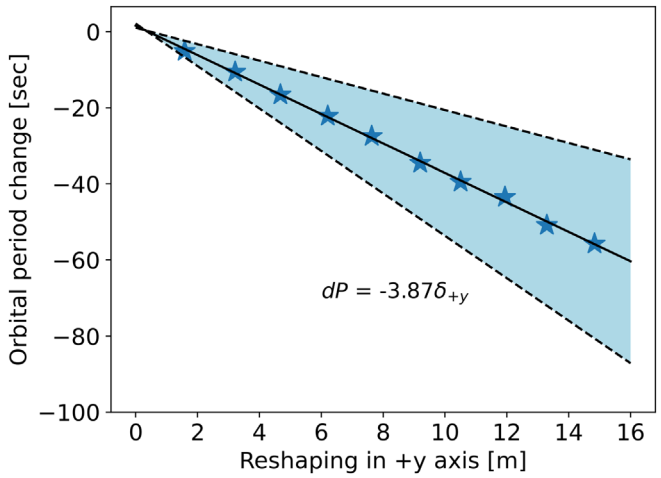

Figure 12. Reshaping in the $+y$-axis (δ_{+y}) vs. orbital period change. The blue stars indicate the simulated results. The black solid line indicates a linear fitted line given by the equation shown in the figure. The blue shaded region represents 1σ in the orbital period change.

Dimorphos's reshaping in the x-axis is very small and negligible (i.e., $\gamma^B_{\pm x} \sim 1$) but its reshaping in the z-axis is relatively large (i.e., $\gamma^B_{\pm z} \neq 1$). We further discuss this in Section 4. Nevertheless, 1.56% suggests that a longer orbital period is unlikely to occur; thus, we conclude that the major effect of Dimorphos's reshaping is to make the orbital period shorter than the nominal case, same as the effect of Didymos's reshaping.

Computing the magnitude of reshaping in the $+y$-axis, δ_{+y}, for each synthetic shape model, we obtain Figure 12, which shows the orbital period change as a function of δ_{+y}. The blue stars are the simulated results and indicate the mean of both the orbital period change and δ_{+y} for 500 shapes for each $\gamma^B_{\max}$ case. We observe that the orbital period linearly decreases as δ_{+y} increases. The linear fitted approximation reads $dP = -3.87\delta_{+y}$. The slope of the equation is less than the case of Didymos's reshaping shown in Figure 9. This suggests that Dimorphos's reshaping has a milder effect on the mutual orbital period compared to Didymos's reshaping for the range of δ_{+y} considered in this work.

4. Discussion

4.1. Postimpact Scenario: Didymos's Reshaping

Given that Didymos should have experienced one or several meteoroid impacts with an impact energy similar to the DART impact (10^{10} J) within the past million years (Jutzi 2015; Richardson et al. 2022), the possibility of a collapse due to the DART impact and other impact-related perturbations is low. However, Didymos's current shape and spin state still give rise to possibility of reshaping. If Didymos is a shattered monolith (although this is not expected), reshaping is unlikely; however, if Didymos is a weak rubble pile, it is likely to be susceptible to impact-related perturbations. Thus, the possibility of reshaping is high. In order to accurately assess the kinetic deflection technique in the event of such reshaping, quantifying the reshaping effect is important.

Using a number of synthetic shape models of the reshaped Didymos, we effectively explored the reshaping conditions and obtained statistically meaningful results. The results of 5000 F2BP simulations revealed that if Didymos reshapes into a more oblate shape (which is its most likely reshaping mode), the orbital period always becomes shorter than the nominal case. Similar results were previously reported by one of the authors (Hirabayashi et al. 2017, 2019), who conducted mutual dynamics simulations by using a second-order inertia-integral model in which the shapes of Didymos and Dimorphos were assumed to be an oblate spheroid and a prolate ellipsoid, respectively. In that study, symmetric reshaping was considered, so only the oblateness (the ratio of the shortest to longest axes) of the spheroid was changed (see Hirabayashi et al. 2019 for more details). Nevertheless, the results showed a shorter orbital period as the oblateness decreases, consistent with the results of the present study. Therefore, we conclude that the orbital period should become shorter, regardless of whether the reshaping is symmetric or asymmetric. This is likely because when Didymos's shape becomes more oblate due to high centrifugal acceleration, its equatorial bulge increases, resulting in a higher J_2 zonal potential harmonic. When J_2 and/or higher-degree terms are present due to nonsphericity, the mass around the equator is effectively greater than the spherical body. This leads to a stronger gravitational attraction on the secondary than the spherical case given by $F = G\frac{m_1 m_2}{r^2}$, where m_1 and m_2 are the masses of the spherical bodies, and r is the separation. The secondary is therefore pulled marginally closer to the primary and orbits faster. This explains why Didymos's reshaping always makes the mutual orbital period shorter than the nominal case.

Importantly, we also found that the orbital period linearly decreases as the reshaping in the z-axis, δ_z, increases (Figure 9). From the determined linear relationship, $dP = -11.12\delta_z$, we can deduce that $\delta_z \geqslant 70$ cm would cause an orbital period change larger than the Earth-based observation accuracy (i.e., $\sim$7.3 s; Rivkin et al. 2021). With the current spacecraft trajectory, the impact will occur on Dimorphos's leading hemisphere, instantaneously reducing the orbital velocity and leading to a shorter orbital period as well (Richardson et al. 2022). Therefore, our results imply that if Didymos's reshaping actually occurs, the Earth-based observations will find an orbital period change larger than the expected orbital period change induced solely by the DART impact, which is $\sim$73 s, assuming that the sole momentum of the projectile is transferred to structurally strong Dimorphos (Rivkin et al. 2021). As a result, β or the contribution of the impact ejecta in its value may be overestimated, potentially giving an erroneous interpretation of the kinetic deflection effectiveness. We thus emphasize that determining whether or not Didymos reshapes after the impact is of critical importance for accurate determination of the DART impact-driven orbital period change and therefore of β.

While it may be difficult to find shape change by comparing light-curve/radar shape models before and after the impact, we anticipate that measuring Didymos's spin period change may help constrain the magnitude of reshaping. This is because, under the assumption that Didymos's angular momentum is conserved at any time, its spin period should change when its moment of inertia is modified by reshaping after the impact. By computing the expected spin period change for each synthetic shape model, we obtain Figure 13, which shows the orbital period change as a function of the spin period change. Notice that the horizontal axis is now the spin period change, instead of the magnitude of reshaping (Figure 9). While the uncertainty in the orbital period change increases as the spin period change

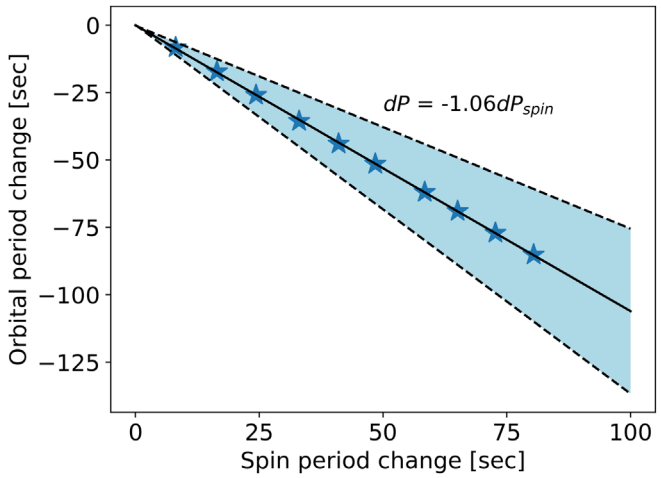

Figure 13. Spin period change vs. orbital period change. For each $\gamma^{A}_{\max}$ case (which has 500 synthetic shape models of the reshaped Didymos), we compute the mean spin period change relative to the nominal case, which is shown by the blue stars. The black solid line indicates the linear fitting of the determined mean values. The blue shaded region indicates 1σ in the orbital period change.

becomes large, the linear relationship still holds. The fitted linear approximation reads $dP = -1.06 dP_{\rm spin}$, where $dP_{\rm spin}$ denotes the spin period change.

Because Didymos's spin period is a quantity that Earth-based telescopes can measure with high precision (an uncertainty of less than 0.1 s by the end of 2023 April; Pravec & Scheirich 2018), measuring the spin period change would, in theory, allow us to constrain reshaping of $\delta_z \geqslant 1$ cm. We can then probe how much reshaping-induced orbital period change needs to be taken into account in the measured orbital period change while waiting for the rendezvous of Hera with the Didymos system, which will fully characterize the physical and dynamical properties of the system in late 2026.

4.2. Postimpact Scenario: Dimorphos's Reshaping

4.2.1. General Effect

We obtained statistically meaningful results for the case of Dimorphos's reshaping too. We found that Dimorphos's reshaping also generally makes the orbital period shorter than the nominal case. The perturbation is relatively milder compared to Didymos's reshaping. This may be because Dimorphos's mass takes only 1% of the system mass; when the reshaping in the $+y$-axis, δ_{+y}, is small and the original shape remains essentially the same as considered in the present study, the mutual gravitational field is modified by a small amount, causing only a small perturbation on the mutual dynamics.

Importantly, however, some limited shapes (78 among 5000 shapes; 1.56%) led to a longer orbital period. We found that this was likely caused by a particular reshaping condition, that is, an almost negligible reshaping in the x-axis but a relatively large reshaping in the z-axis. This suggests that the oblateness and ellipticity of Dimorphos play a role in the mutual orbit perturbation. It is thus worthwhile to investigate the degree 2 zonal and tesseral terms, specifically C_{20} and C_{22}, which encapsulate the dominant reshaping effects on the mutual dynamics. The degree 2 spherical harmonics representation of the gravity potential of a spherical body, V_2, is given by

$$V_2 = -\frac{GM}{r}\left(\frac{a}{r}\right)^2 \sum_{m=0}^{2} P_{2m}\{C_{2m}\cos m\lambda + S_{2m}\sin m\lambda\}, \quad (6)$$

where M is the mass of the body, a is the semimajor axis of a reference ellipsoid, r is the distance from the coordinate origin to the field point, λ is the longitude of the field point, C_{2m} and S_{2m} are the spherical harmonics coefficients of degree 2 and order m, and P_{2m} are the associated Legendre functions of degree 2 and order m. Noting that in the frame aligned with the principal moments of inertia of the body, C_{21}, S_{21}, and S_{22} are identically zero, Equation (6) can be written as

$$\begin{aligned} V_2 &= -\frac{GM}{r}\left(\frac{a}{r}\right)^2 \{P_{20}C_{20} + P_{22}C_{22}\cos 2\lambda\} \\ &= -\frac{GM}{r}\left(\frac{a}{r}\right)^2 \left\{-\frac{1}{2}C_{20} + 3C_{22}\cos 2\lambda\right\}. \end{aligned} \quad (7)$$

Considering V_2 for Dimorphos, the difference in V_2 between the nominal and reshaped cases, δV_2, can then be written as

$$\begin{aligned} \delta V_2 &= V_2^R - V_2^0 \\ &= -\frac{GM}{r}\left(\frac{a}{r}\right)^2 \left\{-\frac{1}{2}(C_{20}^R - C_{20}^0) + 3(C_{22}^R - C_{22}^0)\cos 2\lambda\right\} \\ &= -\frac{GM}{r}\left(\frac{a}{r}\right)^2 \left\{-\frac{1}{2}\delta C_{20} + 3\delta C_{22}\cos 2\lambda\right\}, \end{aligned} \quad (8)$$

where the superscripts 0 and R indicate the quantities for the nominal and reshaped cases, respectively. When $\delta V_2 = 0$, there would be no change in the total mutual potential and thus no orbital period change. In this case, the term inside the curly brackets in Equation (8) becomes

$$\frac{\delta C_{22}}{\delta C_{20}} = \frac{1}{6\cos 2\lambda}. \quad (9)$$

We note that, given the Dimorphos reshaping mode we consider in the present study, δC_{22} is always positive, and δC_{20} and $\cos 2\lambda$ should have the same sign when the equality in Equation (9) is satisfied. On the other hand, when $\delta V_2 > 0$, the total mutual potential of the reshaped case becomes lower than that of the nominal case; thus, the orbital period becomes longer.

In Figure 14, we show the contour plot of the orbital period change (in seconds) as a function of δC_{20} and δC_{22} for 500 shapes in the $\gamma^{B}_{\max} = 1.05$ case. We find that reshaping conditions that fall in the region where $\delta C_{20} \gtrsim 9.5 \times 10^{-3}$ and $C_{22} \lesssim 5.5 \times 10^{-3}$ (bottom right of the contour plot) lead to a longer orbital period. The 0 s contour line can be approximated by a linear line, $\delta C_{22} = 0.3\delta C_{20}$, indicated by the magenta line. Although an offset is present, it is consistent with the blue line, $\delta C_{22} = 0.262\delta C_{20}$, which is obtained from Equation (9), where $\cos 2\lambda$ is set to its mean value. We anticipate that the offset is attributed to the effects of higher-degree zonal and tesseral terms. We thus estimate that the orbital period becomes longer than the nominal case when $\delta C_{22}/\delta C_{20}$ takes a value smaller than 0.3. This holds true for the other $\gamma^{B}_{\max}$ cases. Nevertheless, again, given that the longer orbital period cases were rarely found in the 5000 F2BP simulation results, we conclude that

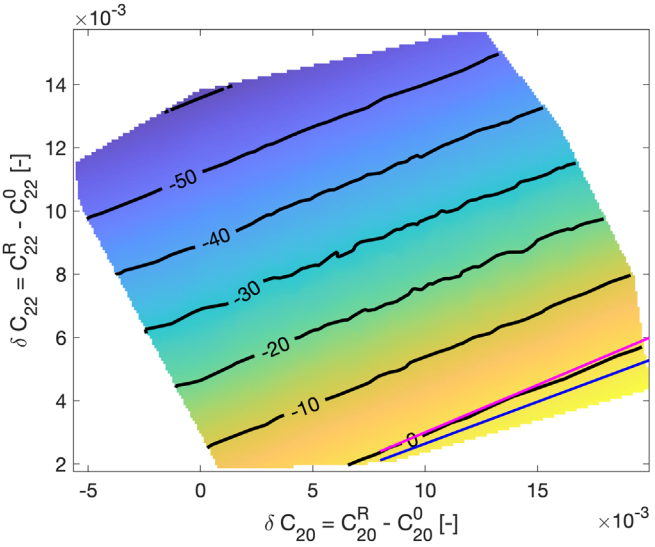

Figure 14. Contour plot of the orbital period change as a function of δC_{20} and δC_{22}. The contour line labels indicate the orbital period change in seconds relative to the nominal case. The magenta line is given by $\delta C_{22} = 0.3\delta C_{20}$. The blue line is given by $\delta C_{22} = 0.262\delta C_{20}$, which is obtained from Equation (9).

the general effect of Dimorphos's reshaping is to reduce the orbital period.

The determined linear relationship between the orbital period change and δ_{+y}, $dP = -3.87\delta_{+y}$ (Figure 12), suggests that if Dimorphos reshapes larger than 2 m in its $+y$-axis, the resulting orbital period change will be larger than the Earth-based observation accuracy (i.e., ∼7.3 s; Rivkin et al. 2021). Again, if such reshaping occurs, the Earth-based observation will find an orbital period change larger than the expected (i.e., ∼73 s; Rivkin et al. 2021), leading to an overestimation of β and/or the contribution of the impact ejecta in its value. Therefore, determining the shape change is also important for Dimorphos, as for Didymos.

Unlike the case of Didymos, however, it is likely going to be difficult to detect Dimorphos's shape change because Dimorphos's shape and attitude dynamics are not resolved by light-curve and radar observations. We suspect that Dimorphos's reshaping magnitude may potentially be estimated by computing the amount of volume displaced by the DART impact based on the total ejecta mass measurements through Earth-based observations and LICIACube (Richardson et al. 2022; Hirabayashi et al. 2022; Fahnestock et al. 2022); however, this requires further assessment and is left for future work. The most accurate β will be obtained by the Hera mission and its full characterization of Dimorphos during its rendezvous with the Didymos system in late 2026 (Michel et al. 2022).

It is important to mention that a recent study suggests that Dimorphos's elongation would affect the libration amplitude, and that the libration may get excited after the DART impact (Agrusa et al. 2021; Ćuk et al. 2020). In the present study, we considered small reshaping ($\delta_{+y} \lesssim 15$ m), so the synthetic shape models had axis ratios (elongation) similar to the original shape model. Therefore, we did not find significant libration excitation. However, if Dimorphos reshapes by a large amount and its shape becomes no longer similar to the original shape, its attitude dynamics will be significantly perturbed, and a so-called "barrel instability" may be triggered (see discussion below).

4.2.2. Effects of a Crater and Global Deformation

We have modeled Dimorphos's reshaping by modifying Dimorphos's semiaxis lengths. However, it is possible that a well-defined crater is formed on Dimorphos's leading hemisphere, where the DART impact takes place (e.g., Stickle et al. 2017, 2022; Rainey et al. 2020; Raducan et al. 2019, 2020). On the other hand, a recent numerical work using the smoothed particle hydrodynamics impact code (Jutzi et al. 2008; Jutzi 2015) suggests a possibility that Dimorphos experiences a process dissimilar to cratering, namely, a global deformation after the DART impact. (See Raducan & Jutzi 2022 for details.) Given these potential outcomes, we conduct two additional investigations in which we use synthetic shape models of (1) Dimorphos with a crater and (2) Dimorphos under global deformation. Below, we summarize these two investigations and show that the effects of both a crater and global deformation are generally the same as the effect of small reshaping ($\delta_{+y} \lesssim 15$ m). However, global deformation could significantly modify Dimorphos's attitude dynamics.

1. *Dimorphos with a crater*—We assume that a crater is formed at the center of the figure of Dimorphos's leading hemisphere by the idealized impact (i.e., Figure 5). Five different crater diameters are considered: 20, 40, 60, 80, and 100 m. Based on earlier studies (e.g., Melosh 1989), the crater's depth-to-diameter ratio is set to 0.1. Given these crater morphologies, we generate five synthetic shape models. Similar to the process outlined in Section 2.2.3, we impose the following three assumptions: (1) Dimorphos's volume remains constant before and after the crater formation, (2) the $-y$-axis is unaffected by the impact (i.e., $-y_0 = -y_1$), and (3) the x- and z-axes are proportionally (symmetrically) increased under constant volume (i.e., $\gamma^B_{\pm x} = \gamma^B_{\pm z}$). Figure 15(a) depicts an example of a synthetic shape model of Dimorphos with a crater.

   We propagate the mutual dynamics for 180 days by using F2BPFEM for each shape. The initial conditions and physical parameters are the same as in Table 1 but with slight modifications to take into account the moment of inertia change. The result shows that the relative angular deviation for the case of the 100 m crater reaches ∼22° at $t = 180$ days, which corresponds to −6.9 s of the orbital period change (Figure 15(b)). This amount of orbital period change is equivalent to that caused by $\delta_{+y} \sim 2$ m reshaping. The smaller (20, 40, 60, and 80 m) craters also make the orbital period shorter; however, the change is small, in a range from ∼−0.5 to ∼−2.5 s, and we find no systematic trend in the relationship between the orbital period change and crater diameter. This suggests that the orbital period change of less than ∼2.5 s may be within the uncertainty of F2BPFEM. Dimorphos's mass distribution should change when a crater is formed; however, the mass distributions for the 20, 40, 60, and 80 m crater cases are almost identical, which cannot be clearly resolved by F2BPFEM, resulting in a similar relative angular deviation evolution as observed in Figure 15(b). A more detailed investigation of the effect of a small crater is left for future work. We note that the attitude dynamics of Dimorphos do not get excited for the range of crater diameters considered here. The libration

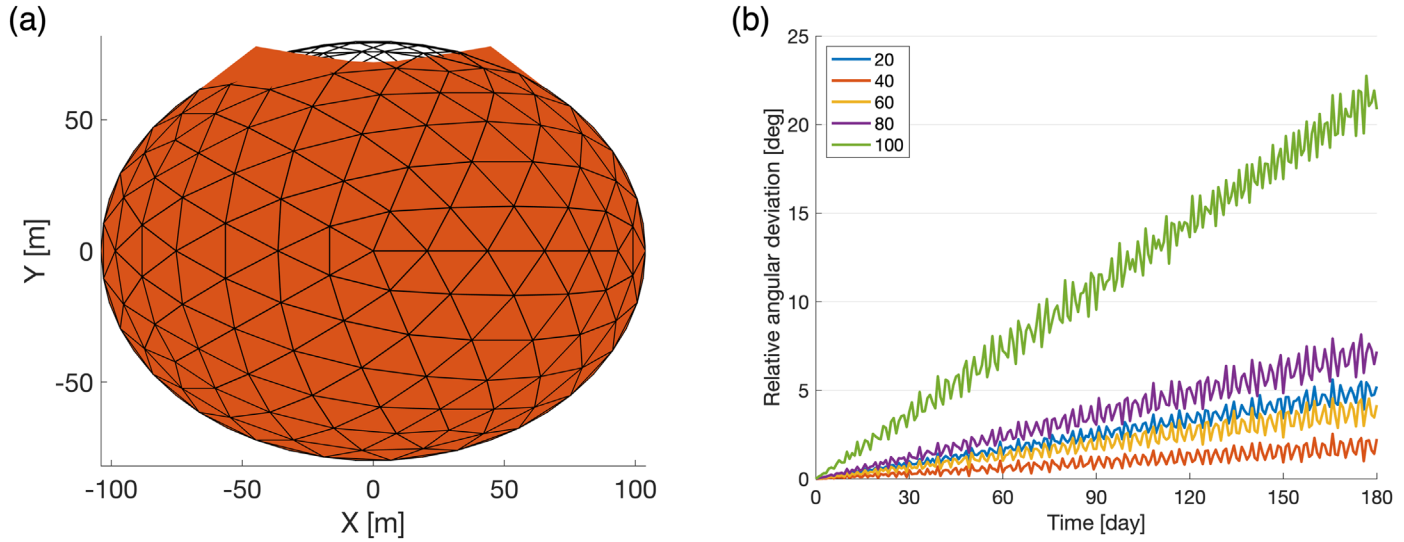

Figure 15. (a) Synthetic shape model of Dimorphos with a 100 m diameter crater (top-down view). The black wire frame represents the original shape. (b) Evolution of the relative angular deviation. The legend specifies the line color for each crater diameter.

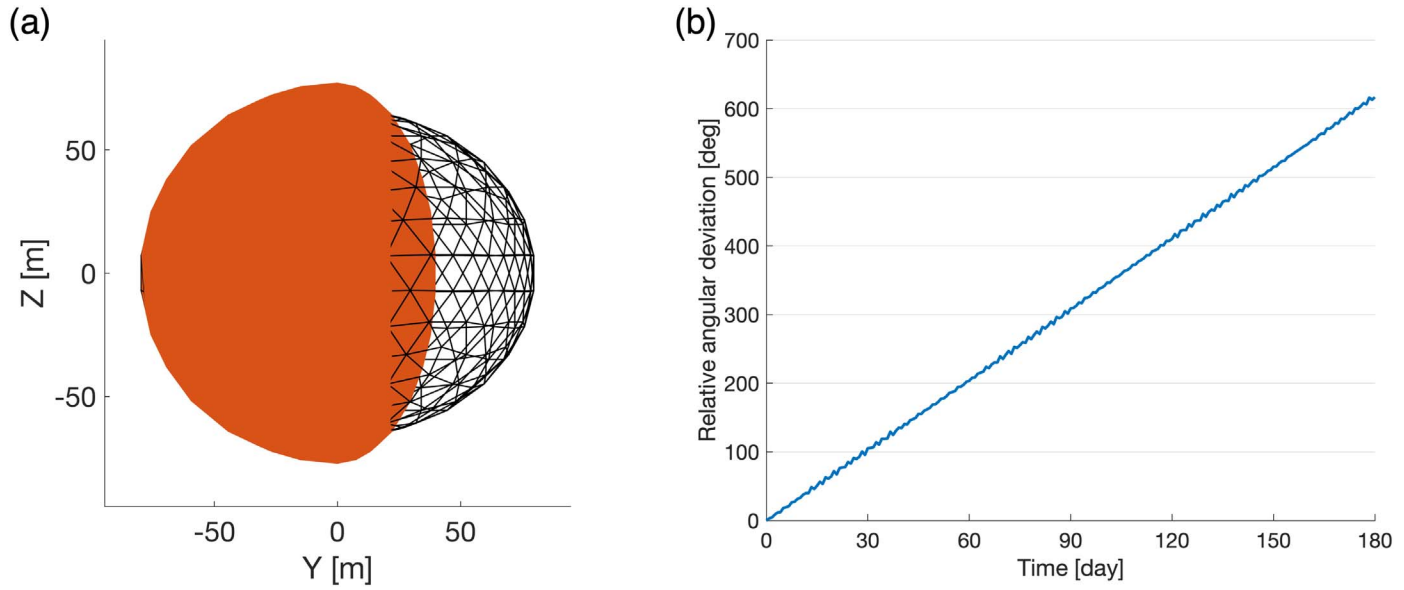

Figure 16. (a) Synthetic shape model of the globally deformed Dimorphos (side view). The black wire frame represents the original shape. (b) Evolution of the relative angular deviation.

amplitudes are generally the same as the nominal case.

In summary, the results suggest that a crater with a diameter of $\geqslant$100 m (which is equivalent to $\delta_{+y} \gtrsim 2$ m) would lead to an orbital period change comparable to the observation accuracy. The effect of a smaller crater is somewhat uncertain but most likely small, i.e., below the observation accuracy. Therefore, we anticipate that the mutual dynamics of the Didymos system (and thus the orbital period) will be generally unaffected as long as the crater diameter is smaller than 100 m.

2. *Dimorphos under global deformation*—To generate a synthetic shape model of a globally deformed Dimorphos, we set $\gamma^B_{+y} = 0.5$ and $\gamma^B_{-y} = 1$, which corresponds to $\delta_{+y} = \sim$40 m. We again assume the constant volume condition and $\gamma^B_{\pm x} = \gamma^B_{\pm z}$. The resulting synthetic shape model is shown in Figure 16(a). Note that this synthetic shape model is consistent with the simulated postimpact shape reported in Raducan & Jutzi (2022).

Propagating the mutual dynamics using F2BPFEM, we find that the relative angular deviation still linearly evolves, but much faster, compared to any of Dimorphos's reshaping conditions considered in the present study. It reaches $\sim$620° at $t = 180$ days, which implies that a globally deformed Dimorphos would be more than one orbit ahead of where the nominal Dimorphos would be (Figure 16(b)). The corresponding orbital period change is ~ -200 s. This result indicates that even though Dimorphos's mass accounts for only $\sim$1% of the total system mass, if global deformation occurs, the mutual gravitational field is greatly modified, leading to a large orbital period change. Importantly, if Dimorphos experiences a global deformation, it implies that its structure is weak (Raducan & Jutzi 2022; Stickle et al. 2022). Then, it is possible that the

orbital period change caused solely by the DART impact would also be significantly larger than ∼73 s, resulting in a larger β than expected based on impact modeling (i.e., in the range 1–5; Stickle et al. 2022).

We also find that Dimorphos's attitude dynamics is greatly perturbed due to global deformation. Specifically, while Dimorphos's major axis generally remains pointing toward Didymos, Dimorphos rolls about the major axis. We find that Dimorphos is in this intermediate rotational state between a tidally locked synchronous state and a chaotic tumbling state, called the "barrel instability" (Ćuk et al. 2020), throughout 180 days of simulation. The barrel instability is thought to terminate BYORP; therefore, if the current secular semimajor axis evolution rate, $\dot{a} = -0.076$ cm yr^{-1} (Scheirich & Pravec 2009; Agrusa et al. 2021), changes significantly after the impact, it potentially suggests that Dimorphos entered barrel instability due to the DART impact (Agrusa et al. 2021) and/or global deformation. It is important to note, however, that the mutual dynamics perturbation due to the DART impact and/or Didymos's reshaping, as well as the resulting change in tidal effect, may similarly result in a change in $\dot{a}$. Further investigation is thus necessary to constrain the secular effects of reshaping and global deformation, and again, clearly constraining Dimorphos's attitude dynamics will require postimpact measurements by the Hera mission (Michel et al. 2022).

5. Conclusion

We investigated how reshaping of Didymos and Dimorphos perturbs the mutual dynamics and changes the mutual orbital period. Based on earlier studies of top-shaped asteroids' structural conditions (e.g., Hirabayashi 2015; Nakano & Hirabayashi 2020) and recent impact modeling work (e.g., Raducan & Jutzi 2022; Stickle et al. 2022), we inferred the most likely reshaping modes of the bodies. Then, we generated 5000 synthetic shape models for each body and conducted a total of 10,000 F2BP simulations using F2BPFEM. We found that both Didymos's and Dimorphos's reshaping would generally make the orbital period shorter than the nominal case; only limited Dimorphos reshaping conditions resulted in a longer orbital period. The orbital period change increased linearly as the magnitude of reshaping increased, from which we deduced that Didymos's reshaping with $\delta_z \geqslant 70$ cm for the case of Didymos's reshaping and $\delta_{+y} \geqslant 2$ m for the case of Dimorphos's reshaping would cause an orbital period change measurable by Earth-based telescopes (i.e., $\geqslant 7.3$ s; Rivkin et al. 2021). Because the DART impact will also reduce the orbital period, the Earth-based observations may find an orbital period change larger than the anticipated orbital period change induced solely by the impact, if reshaping does actually occur. The determined linear relationships are key to decoupling the impact- and reshaping-induced orbital period changes. We anticipate that the effects are independent to first order; thus, constraining Didymos's and Dimorphos's reshaping magnitudes would allow us to determine the impact-induced orbital period change to estimate a reliable β. We discussed that Didymos's reshaping may be constrained by observing Didymos's spin period change. It is likely going to be difficult to constrain Dimorphos's reshaping through Earth-based observations; however, measuring the total ejecta mass to compute the amount of volume displaced by the DART impact may help estimate it. The most accurate β shall be obtained by the ESA Hera mission during its 6 month investigation of the Didymos system starting in late 2026 (Michel et al. 2022).

We also investigated the effects of a crater and global deformation on Dimorphos. We found that a crater with a diameter of less than ∼80 m would only cause an orbital period change smaller than the observation accuracy. Thus, the effect of a crater on the mutual dynamics will be negligible. On the other hand, if global deformation occurs, the orbital period change would be larger than any of Dimorphos's reshaping conditions considered. Furthermore, the barrel instability may be triggered, which potentially terminates BYORP (Ćuk et al. 2020). Detecting the barrel instability through Earth-based observations is likely to be unfeasible; however, Dimorphos's attitude instability may possibly be inferred through detecting a change in the secular orbital evolution rate (e.g., semimajor axis drift) before and after the DART impact.

At present, large uncertainties in the Didymos system's physical parameters pose challenges to making precise predictions of the system' postimpact dynamical and geophysical conditions. As such, we had to impose several assumptions in the present study. Therefore, the present work may not completely describe the true dynamical condition of the Didymos system after the DART impact. However, it highlights the importance of the reshaping effect, which, unless accounted for, can lead to an erroneous determination of the DART impact-driven orbital period change and therefore of β. The techniques and knowledge developed in the present work strengthen our ability to accurately assess the effect of the kinetic deflection technique. As the DART and LICIACube spacecraft approach to the system, the physical parameters and impact conditions will be constrained. It is our future work to conduct further analysis of the postimpact structural and dynamical conditions of the system with updated values, until the Hera spacecraft performs a rendezvous with Didymos in late 2026 and finalizes the required measurements that will eventually offer us a fully documented deflection test.

This work was supported in part by the DART mission, NASA contract 80MSFC20D0004/80NSSC22K0534 to JHU/APL. R.N. acknowledges support from NASA/FINESST (NNH20ZDA001N). P.M. acknowledges support from the French space agency CNES and the European Union's Horizon 2020 research and innovation program under grant agreement No. 870377 (project NEO-MAPP).

Appendix A
Natural Coordinates and Jacobian

To solve Equation (1) by using a bilinear interpolation technique, we employ the tetrahedral natural coordinates. For the element c_k in A, for example, the natural coordinate is defined as (Yu et al. 2019)

$$\delta_{ki} = \frac{A_{ki}}{3V_k}\, \boldsymbol{n}_{ki} \cdot (\boldsymbol{\rho}_A - \boldsymbol{\rho}_{k\bar{i}}), \tag{A1}$$

where i is the corner number, which takes 1–4; V_k is the volume of c_k; A_{ki} is the area of the facet opposite i; $\boldsymbol{n}_{ki}$ is the inward-pointing unit normal vector from the opposite facet; and the subscript $\bar{i}$ indicates any corner that is not i. The natural

coordinates should satisfy

$$\sum_{i}^{4} \delta_{ki} = 1. \tag{A2}$$

Therefore, using three independent coordinates (e.g., δ_{k1}, δ_{k2}, and δ_{k3}), we can specify any point inside of c_k (i.e., $\boldsymbol{\rho}_A$). The Jacobian matrix associated with this transformation is given by (Yu et al. 2019)

$$\frac{\partial(\delta_{k1}, \delta_{k2}, \delta_{k3})}{\partial(x_a, y_a, z_a)} = \frac{1}{3V_k}\begin{pmatrix} A_{k1}\boldsymbol{n}_{k1} \\ A_{k2}\boldsymbol{n}_{k2} \\ A_{k3}\boldsymbol{n}_{k3} \end{pmatrix}. \tag{A3}$$

The Jacobian determinant is found as

$$J_k = \frac{1}{27V_k^3}\prod_{i=1}^{3} A_{ki}|(\boldsymbol{n}_{k1} \times \boldsymbol{n}_{k2}) \cdot \boldsymbol{n}_{k3}|. \tag{A4}$$

Appendix B
Equations of Motion of Full Two-Body Dynamics

Using the FEM expressions for the total attraction force acting on body A, torque acting on body A, and torque acting on body B (Yu et al. 2019), which we denote as $\boldsymbol{f}$, $\boldsymbol{p}$, and $\boldsymbol{q}$, respectively, we can describe the mutual dynamics of a binary asteroid system. The angular momentum of the two bodies is given by

$$\boldsymbol{l}_A = \mathbf{I}_A\boldsymbol{\omega}_A, \qquad \boldsymbol{l}_B = \mathbf{I}_B\boldsymbol{\omega}_B, \tag{B1}$$

where $\mathbf{I}_A$ and $\mathbf{I}_B$ are the moment of inertia tensor of A and B, respectively, and $\boldsymbol{\omega}_A$ and $\boldsymbol{\omega}_B$ are the angular velocity of A and B, respectively. Then, with the symbols given in Table 2, we can write the equations of motion as

$$m_A\dot{\boldsymbol{v}}_A = \boldsymbol{f}, \qquad \dot{\boldsymbol{r}}_A = \boldsymbol{v}_A, \tag{B2}$$

$$\dot{\boldsymbol{l}}_A = \boldsymbol{l}_A \times \boldsymbol{\omega}_A + \boldsymbol{p}, \qquad \dot{\lambda}_A = \frac{1}{2}\lambda_A \diamondsuit \boldsymbol{\omega}_A, \tag{B3}$$

$$m_B\dot{\boldsymbol{v}}_B = -\boldsymbol{f}, \qquad \dot{\boldsymbol{r}}_B = \boldsymbol{v}_B, \tag{B4}$$

$$\dot{\boldsymbol{l}}_B = \boldsymbol{l}_B \times \boldsymbol{\omega}_B + \boldsymbol{q}, \qquad \dot{\lambda}_B = \frac{1}{2}\lambda_B \diamondsuit \boldsymbol{\omega}_B, \tag{B5}$$

where m_A and m_B are the mass of A and B, and λ_A and λ_B are the attitude quaternions of A and B, respectively (Zhao & Van Wachem 2013; Yu et al. 2019). The $\diamondsuit$ operator defines the multiplication between a quaternion and a vector (Hand & Finch 1998). Note that Equations (B2) and (B4) are described in the inertial frame, whereas Equations (B3) and (B5) are described in their body-fixed frames.

Appendix C
Orbital Period Change Computation

Once the relative angular deviation is determined (e.g., Figure 7), we can compute the corresponding orbital period change. Assuming a circular orbit, the orbital velocities of the nominal and reshaped Dimorphos cases are, respectively, described as

$$v_0 = \frac{2\pi}{T_0}, \qquad v = \frac{2\pi}{T}, \tag{C1}$$

where T_0 is the nominal orbital period, and T is the orbital period of the reshaped Dimorphos. Note that, strictly speaking, T and T_0 are time-variant; however, we consider the average values. We also note that the circular orbit assumption is employed, as the eccentricity is expected to remain small (on the order of 10^{-2}–10^{-3}) after the DART impact (Richardson et al. 2022); however, if the mutual orbit is significantly modified by the impact and the eccentricity becomes nonnegligible, the assumption may no longer hold. The angular positions at $t = t_f$ are, respectively,

$$\phi_0 = \int_0^{t_f} v_0\, dt \approx v_0 t_f, \tag{C2}$$

$$\phi = \phi_0 + \delta\phi = \int_0^{t_f} v\, dt = \int_0^{t_f} (v_0 + \delta v)\, dt \approx v_0 t_f + \delta v t_f, \tag{C3}$$

where $\delta\phi$ denotes the relative angular deviation, and δv denotes the relative orbital velocity. From Equation (C3), the relative orbital velocity is written as

$$\delta v = \frac{\delta\phi}{t_f}. \tag{C4}$$

Finally, the orbital period change is given by

$$\delta T = T_0 - T = T_0 - \frac{2\pi}{v_0 + \delta v} = T_0 - \frac{2\pi}{\frac{2\pi}{T_0} + \frac{\delta\phi}{t_f}}, \tag{C5}$$

where the nominal orbital period T_0 is reported as 11.92 hr (Naidu et al. 2020); thus, we can obtain the orbital period change by knowing the relative angular deviation $\delta\phi$ and t_f.

ORCID iDs

Ryota Nakano https://orcid.org/0000-0002-9840-2416
Masatoshi Hirabayashi https://orcid.org/0000-0002-1821-5689
Harrison F. Agrusa https://orcid.org/0000-0002-3544-298X
Fabio Ferrari https://orcid.org/0000-0001-7537-4996
Alex J. Meyer https://orcid.org/0000-0001-8437-1076
Patrick Michel https://orcid.org/0000-0002-0884-1993
Sabina D. Raducan https://orcid.org/0000-0002-7478-0148
Paul Sánchez https://orcid.org/0000-0003-3610-5480
Yun Zhang https://orcid.org/0000-0003-4045-9046

References

Agrusa, H. F., Gkolias, I., Tsiganis, K., et al. 2021, Icar, 370, 114624
Agrusa, H. F., Richardson, D. C., Davis, A. B., et al. 2020, Icar, 349, 113849
Agrusa, H. F., Ferrari, F., Zhang, Y., et al. 2022, PSJ, submitted
Cheng, A. F., Rivkin, A. S., Michel, P., et al. 2018, P&SS, 157, 104
Cheng, A. F., Stickle, A. M., Fahnestock, E. G., et al. 2020, Icar, 352, 113989
Ćuk, M., & Burns, J. A. 2005, Icar, 176, 418
Ćuk, M., Jacobson, S., Walsh, K., et al. 2020, in 14th Europlanet Science Congress, EPSC2020–983
Davis, A. B., & Scheeres, D. J. 2020, Icar, 341, 113439
Davis, A. B., & Scheeres, D. J. 2021, GUBAS: General Use Binary Asteroid Simulator, Astrophysics Source Code Library, ascl:2107.013
Dotto, E., Della Corte, V., Amoroso, M., et al. 2021, P&SS, 199, 105185
Fahnestock, E. G., Cheng, A. F., Ivanovski, S., et al. 2022, PSJ, submitted
Fahnestock, E. G., & Scheeres, D. J. 2006, CeMDA, 96, 317
Fang, J. 2011, AJ, 143, 24
Gao, Y., Yu, Y., Cheng, B., & Baoyin, H. 2022, AdSpR, 69, 2305
Goldreich, P., & Sari, R. 2009, ApJ, 691, 54
Hand, L. N., & Finch, J. D. 1998, Analytical Mechanics (1st ed.; Cambridge: Cambridge Univ. Press)

Hirabayashi, M. 2015, MNRAS, 454, 2249
Hirabayashi, M., Davis, A. B., Fahnestock, E. G., et al. 2019, AdSpR, 63, 2515
Hirabayashi, M., Ferrari, F., Jutzi, M., et al. 2022, PSJ, 3, 140
Hirabayashi, M., Nakano, R., Tatsumi, E., et al. 2020, Icar, 352, 113946
Hirabayashi, M., & Scheeres, D. J. 2013, CeMDA, 117, 245
Hirabayashi, M., & Scheeres, D. J. 2014, ApJL, 798, L8
Hirabayashi, M., Schwartz, S. R., Yu, Y., et al. 2017, MNRAS, 472, 1641
Jutzi, M. 2015, P&SS, 107, 3
Jutzi, M., Benz, W., & Michel, P. 2008, Icar, 198, 242
Maciejewski, A. J. 1995, CeMDA, 63, 1
Melosh, H. J. 1989, Impact Cratering: A Geologic Process (New York: Oxford Univ. Press)
Meyer, A. J., Gkolias, I., Gaitanas, M., et al. 2021, PSJ, 2, 242
Michel, P., Cheng, A., Küppers, M., et al. 2016, AdSpR, 57, 2529
Michel, P., Kueppers, M., Sierks, H., et al. 2018, AdSpR, 62, 2261
Michel, P., Kuppers, M., Bagatin, A., et al. 2022, PSJ, submitted
Murray, C. D., & Dermott, S. F. 1999, Solar System Dynamics (Cambridge: Cambridge Univ. Press)
Naidu, S., Benner, L., Brozovic, M., et al. 2020, Icar, 348, 113777
Nakano, R., & Hirabayashi, M. 2020, ApJL, 892, L22
Nakano, R., & Hirabayashi, M. 2021, LPSC, 52, 1292
Nakano, R., Hirabayashi, M., Agrusa, H. F., et al. 2020, in AGU Fall Meeting (Washington, DC: AGU), NH037–0004
Pravec, P., & Scheirich, P. 2018, in 42nd COSPAR Scientific Assembly, S.3-4-18
Pravec, P., Scheirich, P., Kušnirák, P., et al. 2006, Icar, 181, 63
Pravec, P., Scheirich, P., Kušnirák, P., et al. 2016, Icar, 267, 267
Raducan, S., Davison, T., & Collins, G. 2020, P&SS, 180, 104756
Raducan, S., Davison, T., Luther, R., & Collins, G. 2019, Icar, 329, 282
Raducan, S. D., & Jutzi, M. 2022, PSJ, 3, 128
Rainey, E. S., Stickle, A. M., Cheng, A. F., et al. 2020, IJIE, 142, 103528
Richardson, D. C., Agrusa, H. F., Barbee, B. W., et al. 2022, PSJ, submitted
Rivkin, A. S., Chabot, N. C., Stickle, A. M., et al. 2021, PSJ, 2, 173
Scheeres, D., McMahon, J., French, A., et al. 2019, NatAs, 3, 352
Scheeres, D. J. 2009, CeMDA, 104, 103
Scheirich, P., & Pravec, P. 2009, Icar, 200, 531
Si, H. 2015, ACM Trans. Math. Software., 41, 1
Stickle, A., Rainey, E., Syal, M. B., et al. 2017, Proc. Eng., 204, 116
Stickle, A. M., Burger, C., Caldwell, W. K., et al. 2022, PSJ, submitted
Tricarico, P. 2008, CeMDA, 100, 319
Watanabe, S., Hirabayashi, M., Hirata, N., et al. 2019, Sci, 364, 268
Werner, R. A., & Scheeres, D. J. 2005, CeMDA, 91, 337
Yu, Y., Cheng, B., Hayabayashi, M., Michel, P., & Baoyin, H. 2019, CeMDA, 131, 1
Yu, Y., & Michel, P. 2018, Icar, 312, 128
Yu, Y., Michel, P., Schwartz, S. R., Naidu, S. P., & Benner, L. A. 2017, Icar, 282, 313
Zhang, Y., Michel, P., Richardson, D. C., et al. 2021, Icar, 362, 114433
Zhang, Y., Richardson, D. C., Barnouin, O. S., et al. 2017, Icar, 294, 98
Zhang, Y., Richardson, D. C., Barnouin, O. S., et al. 2018, ApJ, 857, 15
Zhao, F., & Van Wachem, B. 2013, AcMec, 224, 3091